Collisionless shock heating of heavy ions in SN 1987A

Marco Miceli [1,2]*, Salvatore Orlando[2], David N. Burrows [3], Kari A. Frank[4], Costanza Argiroffi [1,2], Fabio Reale[1,2], Giovanni Peres[1,2], Oleh Petruk[5] and Fabrizio Bocchino[2]

Astrophysical shocks at all scales, from those in the heliosphere up to cosmological shock waves, are typically 'collisionless', because the thickness of their jump region is much shorter than the collisional mean free path. Across these jumps, electrons, protons and ions are expected to be heated at different temperatures. Supernova remnants (SNRs) are ideal targets to study collisionless processes because of their bright post-shock emission and fast shocks, but the actual dependence of the post-shock temperature on the particle mass is still widely debated[1]. We tackle this longstanding issue through the analysis of deep multi-epoch and high-resolution observations, made with the Chandra X-ray telescope, of the youngest nearby supernova remnant, SN 1987A. We introduce a data analysis method by studying the observed spectra in close comparison with a dedicated full three-dimensional hydrodynamic simulation that self-consistently reproduces the broadening of the spectral lines of many ions together. We measure the post-shock temperature of protons and ions through comparison of the model with observations. Our results show that the ratio of ion temperature to proton temperature is always significantly higher than one and increases linearly with the ion mass for a wide range of masses and shock parameters.

Shock waves are abrupt transitions between a supersonic and a subsonic flow which transform bulk kinetic energy into thermal energy by compressing and heating the medium[2]. In the Earth's atmosphere, the width of a shock front is of the order of a few molecular mean free paths. In the rarefied astrophysical environments, however, particle–particle interactions (Coulomb collisions) are typically not sufficient to provide viscous dissipation, and collective effects, such as electromagnetic fluctuations and plasma waves, determine the amount of particle heating at the shock front[3,4]. These conditions derive from the mass, momentum and energy conservation across the shock and predict that the post-shock temperature T depends on the shock velocity v_s as $kT = (3/16)mv_s^2$, where m is the particle mass. In a plasma with different particle species, it is still not clear whether a (partial) temperature equilibration between different species can be reached, or particles with different masses reach temperatures proportional to their mass as

$$kT_i = \frac{3}{16}m_i v_s^2 \qquad (1)$$

where m_i is the particle mass for the ith species. Collisionless shocks have been observed decades ago in the solar wind[5], as well as on cosmological scales[3]. A post-shock temperature proportional to the particle mass is expected in the case of scattering isotropization of the incoming particles by plasma waves. Nevertheless, partial equilibrium between different species is also possible and the applicability of equation (1) for all collisionless shocks is far from settled. Thus, the conditions of the post-shock plasma are still under debate.

Pioneering works have shown the importance of Balmer-dominated shock fronts in SNRs as diagnostic tools[6,7] and the study of the Hα line profile is widely used to measure the electron to proton temperature ratio T_e/T_p (refs. [1,8]). However, this ratio is typically much higher than the electron to proton mass ratio (m_e/m_p) and can increase up to 1 in slow ($v_s \approx 400\,\mathrm{km\,s^{-1}}$) shocks[9,10], showing a dependence on the shock velocity which has been modelled as $T_e/T_p \propto v_s^{-2}$. This can be explained if the immediate electron post-shock temperature does not depend on the shock velocity[11] (and is always $kT_e \approx 0.3\,\mathrm{keV}$), while T_p varies as in equation (1). This behaviour can be associated with a mechanism of electron heating due to lower hybrid waves in a cosmic ray precursor[12], although other scenarios have been proposed[13]. The general expectation is that there can be different plasma instabilities that can enhance T_e/T_p above the expected value m_e/m_p, and the electron heating processes in collisionless shocks are different from those of ions[3,14,15]. Therefore, it is necessary to accurately measure the ion temperatures to test equation (1).

However, the measurement of the post-shock temperatures for different ions has produced different results[8]: the temperature of oxygen ions relative to protons was found to be less than that predicted by equation (1) in the analysis of ultraviolet observations of SN 1006[16], whereas it was found to be higher than equation (1) predicted in interplanetary shocks[17]. Recently, an important result has been obtained in SN 1006, with He, C and N ion temperatures being consistent with the mass-proportional scenario[18]. Stronger constraints need to be obtained by testing equation (1) over a wider range of masses, by inspecting elements heavier than N. To this end, the X-ray band is the ideal window in which bright emission lines of heavy ions are typically observed. Up to now, X-ray spectra have only been used in one case to measure a line broadening of the O VII line triplet, corresponding to an extremely high oxygen temperature (~300 keV) in an isolated ejecta knot of SN 1006[19,20].

SN 1987A in the Large Magellanic Cloud offers a unique opportunity of observing a nearby, young, bright SNR with high level of detail. SN 1987A was a hydrogen-rich core-collapse supernova discovered on 1987 February 23[21]. Its evolution has been extensively covered by a wealth of observations in different wavelengths[22,23] and
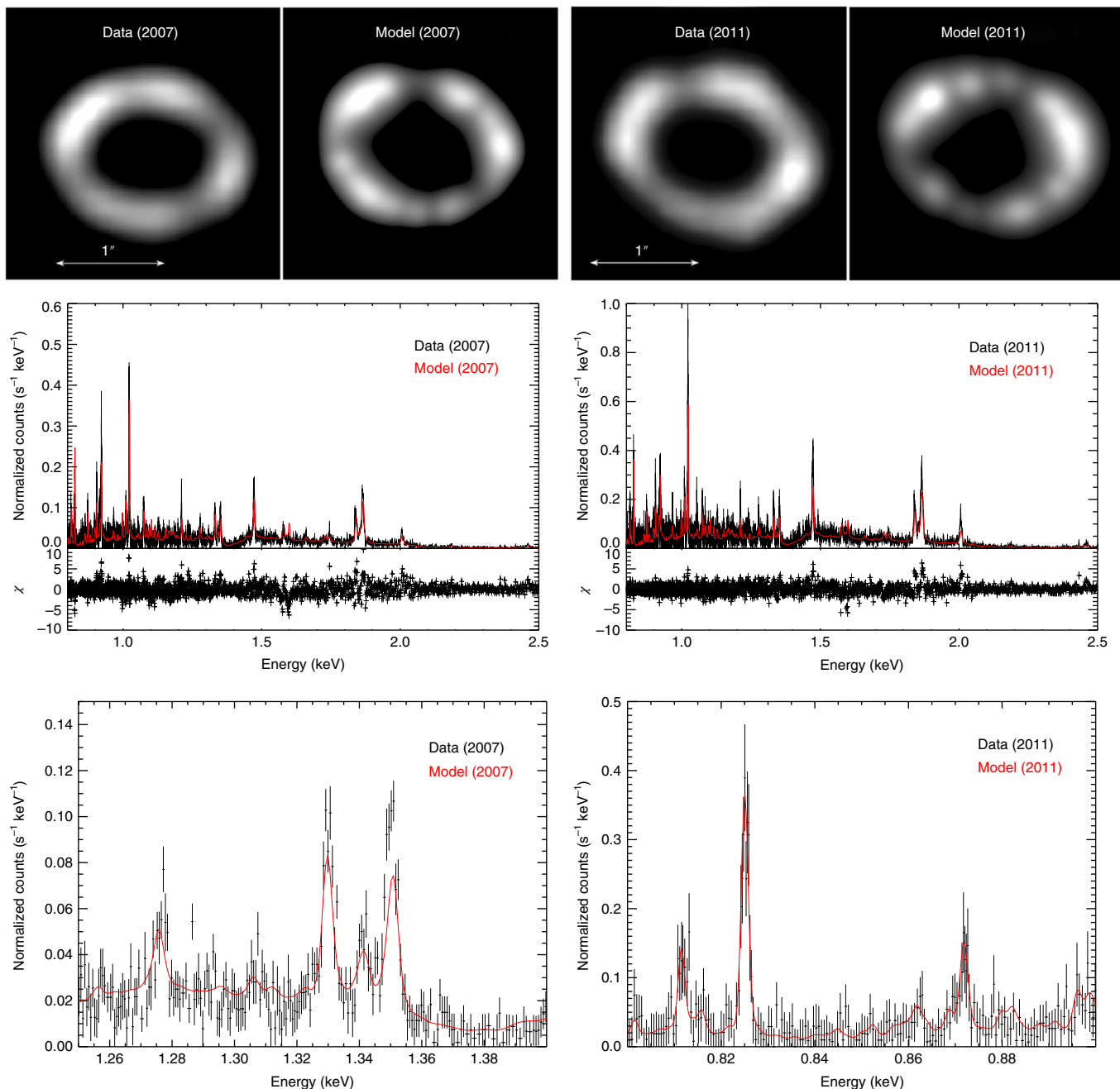
Fig. 1 | Observed and synthetic maps and spectra of SN 1987A. Upper panels: observed and synthetic maps in the 0.5–2 keV band in 2007 (left) and 2011 (right). Central panels: observed (black) and synthetic (red, with all sources of line broadening) spectra in the 0.8–2.5 keV band (MEG +1 diffraction order of the Chandra HETG; error bars are at 1σ) in 2007 (left) and 2011 (right) with the corresponding residuals. Lower panels: close-up views of the central panels in the 1.25–1.4 keV band (in 2007, left) and 0.8–0.9 keV band (in 2011, right).

reveals a complex interaction of the blast wave with the surrounding inhomogeneous medium, characterized by a dense, clumpy ring-like nebula, inside a more diffuse H II region. The interaction with the nebula is best revealed in X-rays, and SN 1987A has been monitored through dedicated campaigns of observations with XMM-Newton and Chandra.

The series of X-ray observations encodes information about the physical properties of both the nebula and the stellar ejecta and requires a thorough data analysis: phenomenological models have only analysed single observations, regardless of the whole succession of data sets. In our new approach, a single 3D hydrodynamic model[24] describes the evolution of SN 1987A from the onset of the

supernova to the current age and accounts self-consistently for all the observations and for the evolution of the system. The reliability of the model has been tested and confirmed by synthesizing light curves, images and low-resolution (charge-coupled device, CCD) spectra from the hydrodynamic simulations. We found that our model self-consistently fits: (i) the bolometric light curve during the first 250 days of evolution, (ii) the soft (0.5–2 keV) and hard (3–10 keV) X-ray light curves in the subsequent 30 years, (iii) the evolution of the morphology of the X-ray emission, and (iv) XMM-Newton EPIC and Chandra ACIS spectra at different epochs[24]. Here we use this forward modelling approach to obtain deeper insight into the physics of shock heating, through the detailed reproduction
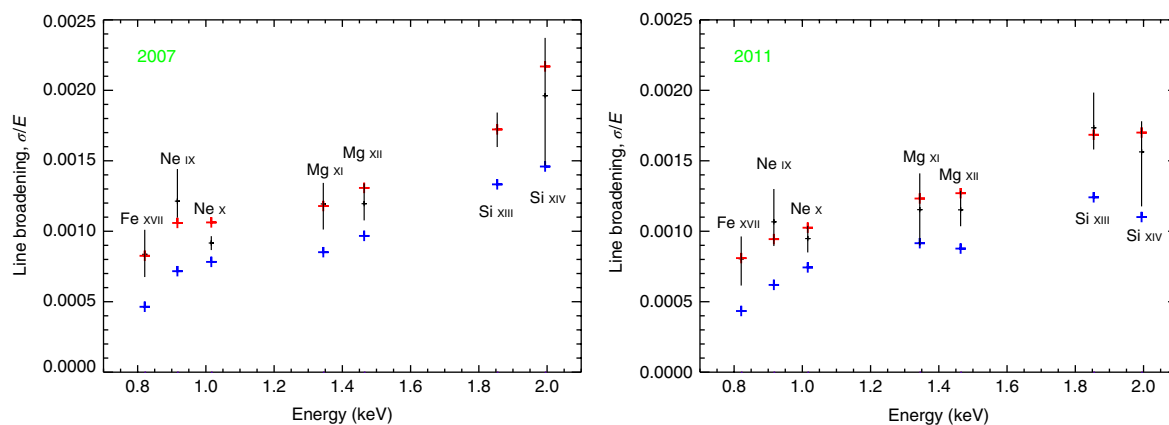
Fig. 2 | Line broadening for selected ions in the X-ray spectra of SN 1987A. Left panel, 2007; right panel, 2011. Black crosses show the observed values (MEG +1 diffraction order of the Chandra HETG). Line broadenings synthesized from our model by considering both Doppler and instrumental broadening are indicated by the blue crosses. Synthetic line broadenings with Doppler, instrumental and thermal broadening are indicated by the red crosses. Error bars are at the 90% confidence level.

of the multi-epoch, high-resolution grating X-ray observations of SN 1987A.

To synthesize the Chandra gratings spectra from the model, we included all the sources of line broadening, namely: (i) the bulk velocities of the different parts of the ring, (ii) the instrumental broadening (due to both line response function and X-ray source extension in the dispersion direction) and (iii) the thermal broadening. To add the contribution of thermal heating in our synthetic spectra, we assumed the ion temperature to be mass-proportional with respect to the proton temperature. The latter is accurately followed by our hydrodynamic code, which includes a detailed model of shock heating[11] and post-shock evolution due to Coulomb collisions between protons and electrons[25] (see Methods for further details). We produced synthetic spectra either with or without thermal broadening. By comparing the synthetic linewidths with those measured in the actual spectra, we were able to infer the role of thermal broadening and its dependence on the ion mass.

We considered the two deepest observations of SN 1987A performed with the Medium Energy Grating (MEG) spectrometer of the Chandra High Energy Transmission Grating (HETG). The two data sets mark two different evolutionary states and different conditions in the shocked plasma: the first consists of a set of 14 exposures performed between March and April 2007 (supernova days 7,321–7,358, total exposure time of 354.9 ks) and corresponds to the initial phase of interaction between the blast wave and the circumstellar ring, whereas in the second one (four HETG exposures, March 2011, 178 ks) the shock has already crossed the bulk of the ring and the X-ray flux is about double that in 2007[26].

The hydrodynamic model simulates the evolution of the ring throughout this time range. Upper panels of Fig. 1 show the observed and synthetic X-ray images of SN 1987A in 2007 and 2011, while central panels show the comparison between the observed high-resolution spectra and the synthetic spectra derived from our hydrodynamic simulations including all the possible sources of line broadening. The model agrees closely with the observations and matches in detail the X-ray spectra in both epochs (reduced $\chi^2 = 1.95$, 1.21 with 2,109 degrees of freedom. in 2007 and 2011, respectively), where emission lines from Fe XVII and He-like and H-like ions of Ne, Mg and Si are visible.

The model reproduces even the significant line broadening of the single lines (lower panels of Fig. 1), which results from a combination of bulk Doppler effects due to the bulk velocities of the approaching and receding parts of the ring, thermal broadening associated with the high temperatures of ions, and instrumental

effects. Previous works neglected thermal broadening and used the linewidths to derive a posteriori the bulk velocity of the plasma[27–29]. Our model provides us with complete information to derive the total line broadening and its evolution in a self-consistent way: that is, all the hydrodynamics and thermodynamics, and the bulk motion of the shocked plasma at all times. In particular, the bulk Doppler broadening depends on the ring and clump densities (which affect the post-shock dragging) and on the density/velocity profiles of the outer ejecta; all these parameters are well constrained by our model. To highlight the contribution of thermal broadening, we compare in Fig. 2 the line broadening derived from the model (either with or without thermal contribution) with the observed linewidths for the two data sets. The figure clearly shows that the line broadening from the model without thermal contribution is large and changes from line to line and in time, as the shock expands through different parts of the ring. Nevertheless, it is always significantly smaller than the observed one—that is, the bulk motion of the gas is not sufficient to explain the observed line broadening.

The linewidths derived from the model by also including the thermal broadening are indicated by the red crosses in Fig. 2 and are in excellent agreement with those observed, for all the ions, and for the 2007 and 2011 observations. Figure 3 shows a close-up view of the Fe XVII line profile to highlight this point.

To quantitatively check whether equation (1) holds for the different ions, we derived the post-shock ion temperatures T_i (Ne, Mg, Si, Fe) through the difference between the observed linewidths and those predicted by the model considering only bulk Doppler broadening and effects of a spatially extended source (black and blue crosses in Fig. 2). The corresponding proton temperatures can be derived from our model. We found that the ion to proton temperature ratio increases monotonically with the ion mass both for the 2007 and the 2011 data sets. Given that the two observations provide consistent results, we combined them, by also combining the results from different ionization states of the same elements to further reduce the error bars.

Figure 4 shows the post-shock Ne, Mg, Si and Fe temperatures normalized to the corresponding proton temperatures. We performed a simple linear regression on the data points in the figure, finding that the ion to proton temperature ratio T_i/T_p increases with the ion mass A as $T_i/T_p = kA$ with $k = 0.90 \pm 0.12$. Therefore, the ion post-shock temperature is consistent with being mass-proportional. This result is in agreement with predictions of hybrid simulations of collisionless shocks[30]. We therefore validate equation (1) over a wide range of masses probing the ion heating mechanism of
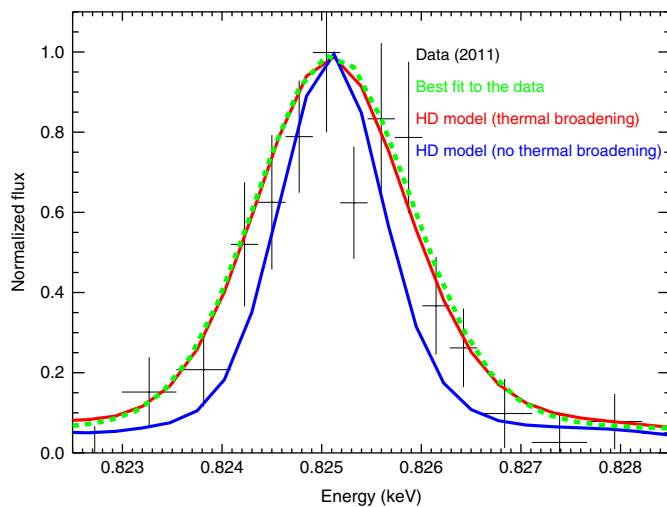
Fig. 3 | Modelled and measured Fe XVII line profile for 2011. Fe XVII line profile derived by our hydrodynamic model for 2011 with (red curve) and without (blue curve) thermal broadening, together with the corresponding 2011 Chandra data (black crosses, showing the error bars at 1σ) and the Gaussian best fit to the data (green dashed curve). HD, hydrodynamic.

Fig. 4 | Ion to proton temperature ratios measured by combining the 2007 and 2011 observations of SN 1987A for Ne, Mg, Si and Fe lines. The red line marks the mass-proportional trend predicted by equation (1), while the black line shows the best-fit trend, with the corresponding 90% confidence range indicated by green lines.

collisionless shocks. By analysing multi-epoch observations performed at different phases of the shock–ring interaction, we also showed that the mass-proportional heating mechanism holds for different shock parameters.

Methods

Proton and electron temperatures in the hydrodynamic model. The model adopted here relies on the combination of a 1D Lagrangian code of the supernova explosion, which simulates the bolometric light curve and time evolution of the photospheric velocity and temperature of SN 1987A during the first 250 days of evolution, and a full 3D hydrodynamic code, which reproduces the expansion of the remnant between days 1 and 15,000 after the supernova[24]. The model set-up, equations and implementation, as well as its capability of reproducing observables, have already been confirmed and discussed elsewhere[24]. We focus here on the treatment of the temperature evolution in the shocked plasma. The proton temperature in the immediate post-shock region is calculated through the canonical equation $kT_p = 3 / 16 \, m_p v_s^2$. Electrons are heated at the shock front up to $kT \approx 0.3$ keV (regardless of the shock Mach number), as suggested[11] for shock velocities of the order of 10^3 km s^{-1}, like those in our simulations (this is crucial, because a mass-proportional heating for the electrons does not allow us to reproduce the observed data with the adopted set-up). We calculate the evolution of proton and electron temperatures in each computational cell of the post-shock medium by considering the effects of the Coulomb collisions in the time $\Delta t = t - t_s$ where t is the current time and t_s is the time when the plasma in each cell was shocked (this is important also to account for the non-equilibrium of ionization effects; see next section). The electron to proton temperature ratio T_e/T_p therefore depends on the shock velocity and on the time elapsed after the shock impact.

Supplementary Fig. 1 shows the distribution of the emission measure of the X-ray emitting plasma in the computational cells (all having the same volume) versus T_e/T_p at $t = 20$ yr and $t = 24$ yr (after the explosion, corresponding to year 2007 and 2011, respectively). The figure reveals the contribution of the dense clumps in the ring (where the shock velocity is relatively low and $T_e/T_p \approx 1$), of the interclump medium within the ring ($T_e/T_p \approx 0.2$–0.6), and of the hotter and relatively tenuous H II region (high shock velocity and $T_e/T_p \approx 0.01$–0.3).

Coulomb collisions can produce variations of T_e from the immediate post-shock value on a short timescale. On the other hand, the evolution of the proton temperature is much slower, and T_p always varies less than 10% with respect to the immediate post-shock values over the time spanned by our simulation. Therefore T_p as well as T_i reflects closely the immediate post-shock conditions in SN 1987A. Over the computational domain, T_e ranges between $\sim 3.5 \times 10^6$ K and $\sim 5 \times 10^7$ K, while T_p is in the range 3.5×10^6 to 8×10^8 K.

Coulomb collisions between different ion species and between ions and protons are not included in our model. From the parameters of our simulations, it is possible to estimate the thermal equilibration timescale for ion and protons[25]. For the ion–ion interactions, the e-folding time for the temperature evolution is of the order of a century, which is much higher than the time elapsed after the shock impact (the shock reached the ring in 2001, and we are looking at the 2007 and
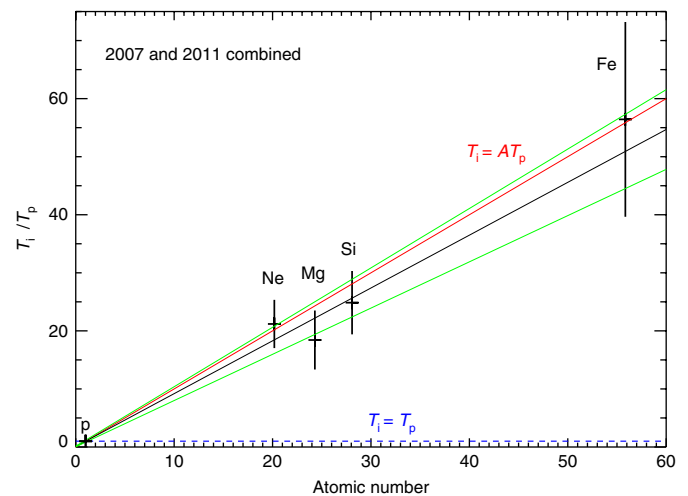
2011 data), so this process is indeed negligible. For the ion–proton interactions, instead, the e-folding time is comparable to the time elapsed after the shock impact. However, for the very turbulent magnetic field that we expect in the post-shock region[31], the thermalization timescale increases[32] by a factor of about 5, thus making this process negligible for our case.

The electron to proton temperature ratio has been measured at the reverse shock of SN 1987A by analysis of observations[33] performed in 2011 (that is, at $t = 24$ yr) by the Cosmic Origins Spectrograph of the Hubble Space Telescope (HST-COS), showing that $T_e/T_p \approx 0.14$–0.35 (this value can change slightly with different assumptions, but $T_e/T_p > 0.1$ is always required to explain the data[33]). We calculated T_e/T_p at the reverse shock from our hydrodynamic model at $t = 24$ yr (corresponding to 2011). We considered only those computational cells that were more than 99% filled with hot ($kT \geq 0.3$ keV) ejecta material. The ejecta material can be identified thanks to a passive tracer included in the calculation[24]. This selection allows us to isolate the shocked (high-temperature) ejecta in the immediate post-shock region (in the post-shock flow, the ejecta are rapidly mixed with the shocked circumstellar medium, and the percentage of ejecta in the computational cells rapidly drops below 99%), thus selecting a narrow sheet of plasma behind the reverse shock. We then computed the density-weighted average value of the electron to proton temperature ratio for these cells, finding $T_e/T_p = 0.155$, in remarkable agreement with that inferred from the observations. This provides a further indication of the reliability of our model.

Synthesis of X-ray spectra. From the model results, we synthesized the Chandra HETG X-ray spectra from the values of T_e, density and ionization timescale (computed on the basis of the plasma density and time elapsed after the shock heating) by adopting the ATOMDB V3.0.8 database. We adopted the VNEI model within XSPEC which requires, as input, T_e and the plasma ionization timescale to compute the continuum and line emission, and followed the same approach as in previous studies[24,34,35]. The X-ray spectrum from each cell was filtered through the photoelectric absorption by the interstellar medium, with the appropriate column density[36]. All synthetic spectra are folded through the Chandra instrumental response. To synthesize the line profiles of the Chandra HETG spectra, we accounted for the three possible sources of line broadening, namely (i) the angular extension and morphology of the source, that is, the position of each X-ray emitting cell in the computational domain, given that the shape of the emission lines depends on the shape of the zero-order spatial structure convolved with the instrumental line spread function, (ii) the Doppler broadening, associated with the bulk velocity of the plasma, and (iii) the thermal broadening, due to the ion temperature, as explained in detail below.

SN 1987A is resolved by the mirrors of Chandra, which clearly show a ring-like morphology for the X-ray-emitting plasma that is very similar to that predicted by our model (see Fig. 1). The morphology of the X-ray emission results from a shocked circular equatorial ring whose symmetry axis is tilted with respect to the line of sight. In our simulation, we assumed the supernova explosion to be at the origin of a 3D Cartesian coordinate system, and the dense equatorial ring on the (x,y) plane. We then rotated the system about the three axes to fit the actual inclination of the ring as found from the analysis of optical data[37], namely $\theta_x = 41°$, $\theta_y = 8°$ and $\theta_z = 9°$. The projected (in the plane of the sky and in the direction

of dispersion) angular distance of each X-ray emitting plasma element from the centre of the ring in the zero-order image determines a wavelength offset corresponding to $\Delta\lambda = 0.01112$ Å per pixel, where the pixel size is $0.492''$, in the Chandra MEG spectra. We therefore included this effect in synthesizing the spectra from the model for each computational cell, by taking into account the actual roll angle of the Chandra observations, where the ±1 arms of the dispersion axis are aligned approximately south/north, respectively. We note that the synthetic zero-order images are about 10% smaller than those observed (Fig. 1) and we verified that this is not an issue for the spectra in the MEG $+1$ diffraction order described here. In fact, if we artificially enhance the angular size of the synthetic maps by about 20% (that is, making them larger than those observed) and compute the line broadening accordingly, the width of the lines increases by <1% for the $+1$ order, thus not affecting our results and conclusions. Although MEG -1-order spectra are more sensitive to this issue, the $+1$-order spectra discussed here do not change significantly. This is because in the $+1$ order, the effects of the angular extension of the source are partly counterbalanced by Doppler effects, as explained below.

We computed the effects of the bulk Doppler broadening associated with the bulk motion of the post-shock plasma in the computational cells by taking into account the inclination of the ring with respect to the line of sight. Supplementary Fig. 2 shows a slice of the plasma velocity along the line of sight, for the X-ray emitting plasma, in the plane identified by the line of sight and the north direction in the sky, at $t = 20$ yr and $t = 24$ yr. The two parts of the ring intercepted by the plane of the cut are visible as indentations with low velocity, in the upper left and lower right parts of the plot. Because the X-ray emission scales as the square of the particle density, we also plot the corresponding cuts of density to show the different weight (for the emerging spectrum) of the plasma velocities in different regions of the model. On changing the value of θ_x by $\pm5°$ (that is, more than the observational uncertainty on this parameter[37]), the width of the synthetic lines changes only by <0.5% in the $+1$ order, thus leaving all our conclusions unaffected. Because of the inclination of the ring with respect to the line of sight, as the shock expands, the X-ray emission of the plasma in the northern part of the ring will be, on average, blueshifted, while that originating in the southern part of the ring will be redshifted. Since in the $+1$ order the dispersion axis is pointing south, the effects of bulk Doppler broadening and of the angular extension of the source work in opposite directions, whereas they sum in the -1 order (whose dispersion axis points north). Therefore, the combined effects of the source angular extension and of Doppler broadening make the emission lines broader in the -1 order than in the $+1$ order, as already pointed out[27,28,38] for the analysis of the actual Chandra spectra. Because of this, the relative contribution of thermal broadening (which is, in absolute, the same in the ±1 orders) to the total line broadening will be higher in the $+1$ spectra.

As explained in the previous section of the Methods, we followed the evolution of T_p and T_e in the post-shock flow. Electron temperature, together with ionization timescale, plasma density and bulk velocity, allow us to synthesize the emerging X-ray spectrum from each computational cell, while the local value of T_p allows us to derive the thermal line broadening, as explained below. To include the effects of thermal broadening, we consider the values of T_p in each cell and assume that ions with atomic mass A have temperature $T_i^{\text{mod}} = A T_p$, as in equation (1). On the basis of our assumption, we can add in quadrature a Gaussian broadening with

$$\sigma_{\text{th}} = E\sqrt{\frac{kT_i^{\text{mod}}}{m_i c^2}} = E\sqrt{\frac{kT_p}{m_p c^2}} \qquad (2)$$

where E is the energy of the emission line, k is the Boltzmann constant, and c the speed of light. In this way, from T_p we can synthesize from our simulations the line broadening expected in case of mass-proportional post-shock temperature. We then compare the synthetic line broadening with that observed to test the mass-proportional assumption against actual observations (Sect. M4).

We fitted the synthetic line profiles with Gaussians to measure their widths. The widths for selected emission lines in the $+1$ order spectra obtained either with (red crosses) or without (blue crosses) thermal broadening at $t = 20$ yr and $t = 24$ yr are shown in Fig. 2, while Supplementary Fig. 3 shows the widths for the -1 order at $t = 24$ yr. As expected, the total line broadening is higher in the -1 order, and this makes the estimate of ion and proton temperatures difficult when comparing models and observations (see 'Diagnostics' section below).

Data analysis. We analysed Chandra observations 7588–90, 8487, 8488, 8523, 8537–9, 8542–6 (PI C. Canizares) performed between March and April 2007 with a total exposure time of 354.9 ks, and observations 12145, 12146, 13238, 13239 (PI C. Canizares) performed on March 2011 for a total exposure time of 178 ks. All observations have pointing coordinates $\alpha_{\text{J2000}} = 05$ h 35 min 28.0 s, $\delta_{\text{J2000}} = -69° 16' 11.0''$ and were reprocessed with CIAO 4.9 and CALDB 4.7.3.

We extracted the MEG ±1 spectra by producing the corresponding auxiliary response file, ARF (with the *fullgarf* script) and redistribution matrix file, RMF (with the *mkgrmf* script) files. We then combined all the 14 spectra of the same order for the 2007 exposures and the four spectra of the same order for the 2011 exposures by using the *combine_grating_spectra* script in CIAO, thus obtaining cumulative $+1$ order and -1 order MEG spectra for the two epochs.

Spectral analysis has been performed with XSPEC V12.9.1. We fitted the single lines in narrow bands by adopting Gaussian components plus a thermal bremsstrahlung component (to fit the continuum). We also included the interstellar absorption (TBABS model within XSPEC) in all the spectral fittings, by fixing the absorbing column density to $N_H = 2.35 \times 10^{21}$ cm^{-2}, in agreement with previous works[36]. As explained above, we measure higher linewidths in the -1 order than in the $+1$ order. The best-fit parameters are shown in Supplementary Table 2.

Diagnostics from the comparison between models and observations. The procedure adopted to compare models and data is summarized in the flow chart shown in Supplementary Fig. 5 and described below. First, from our hydrodynamic simulations, we synthesize X-ray spectra without including the effects of thermal broadening and compare them against the Chandra data. These synthetic spectra severely underestimate the observed line broadening (both in 2007 and 2011), as shown in Fig. 2. This proves that bulk Doppler broadening and spatial extension of the source cannot reproduce the total observed line widths, and an additional source of broadening, associated with high ion temperatures, is necessary to explain the data. We therefore measure the ion temperatures in SN 1987A from the difference between the observed linewidths and those predicted by the model considering Doppler and spatial effects only (all the linewidth contributions are summed/subtracted in quadrature).

Then we checked whether the model reproduces the observed linewidths by including the effects of thermal broadening in the synthesis of emission. In doing this, we considered the values of T_p in each cell and assumed a mass-proportional ion temperature—that is, that ions with atomic weight A have temperature $T_i^{\text{mod}} = A T_p$, as explained in the section 'Synthesis of X-ray spectra' above. Figure 2 shows that the widths of the emission lines measured in the Chandra spectra (for both the 2007 and 2011 observations) are in excellent agreement with the predictions. It is worth noting that if we assume $T_i^{\text{mod}} = T_p$ the model fails in reproducing the observed linewidths. The capability of our synthetic spectra to reproduce the multi-epoch line broadening both in the $+1$ order (where the contribution of thermal broadening is higher) and in the -1 order (where the bulk Doppler broadening dominates over thermal broadening; see 'Synthesis of X-ray spectra') indicates that we are correctly estimating the bulk Doppler broadening and that our results are robust.

The agreement between model predictions and multi-epoch observations strongly confirms the predictions of equation (1) and proves that ions are heated up to higher temperatures than protons, according to their mass. If ions were only heated to temperature T_p (that is, by assuming thermal equilibration between particle species at the shock front), the thermal width of their emission lines would not be enough to explain the observed broadening, being reduced by a factor ranging from ~4.5 (for Ne) up to ~7.5 (for Fe), as explained by equation (2).

To quantify the agreement between equation (1) and our joint modelling and data analysis of SN 1987A, we produced the plot shown in Fig. 4. To this end, we use the value of T_i deduced from the comparison between actual spectra and those synthesized from the model without including thermal broadening, and the corresponding proton temperature calculated from our hydrodynamic simulations, as explained below. The global X-ray spectrum of SN 1987A forms from a very broad distribution of emission measure versus temperature (see Supplementary Fig. 1), and different emission lines arise from plasma at different (electron and proton) temperatures. 'Colder' lines (for example Fe xvii and Ne ix) originate where the plasma temperature is lower (generally, behind slow shocks such as those propagating in the clumps), whereas 'hotter lines' (for example Si xiv) stem from high-temperature regions. This calls for the need to estimate the average emission-weighted proton temperature $\overline{T_p}(l)$ from the plasma contributing to each emission line (the index l runs over all the inspected lines). This is possible by comparing our synthetic spectra obtained with and without thermal broadening. In fact, the separation between red and blue crosses in Fig. 2 depends on T_i^{mod} and provides a measure of the emission-weighted average value (the average being calculated over all the domain) of ion temperature for each line, $\overline{T_i^{\text{mod}}}(l)$, and then on $\overline{T_p}(l)$ (through equation (2)). We thus obtain the proton temperatures listed in Supplementary Table 1 for each line in the $+1$ order spectrum. The temporal evolution of the average $\overline{T_p}$ in the different emission lines is non-trivial, depending on the expansion of the shock (that is, contribution from newly shocked plasma), on the temporal evolution of T_e and T_p due to the Coulomb collisions, on the mixing of different plasma components, and on the complicated evolution of the distribution of emission measure (and particle density) versus temperature and ionization timescale.

We then divided T_i (calculated by comparing observations and synthetic spectra without thermal broadening) by the corresponding $\overline{T_p}$ (inferred from the model as explained above) and obtained the results shown in Supplementary Fig. 4. For all lines, in both epochs, T_i is always significantly higher than the proton temperature, a result that is reliable as it depends on shock velocities and plasma densities that are well constrained by our simulation[24]. We then averaged the ion to proton temperature ratios for He-like and H-like ions of the same species and obtained the results shown in the right panels of Supplementary Fig. 4, for 2007 (upper panel) and 2011 (lower panel). As the two epochs provide consistent results, we further reduced the error bars by combining them, thus obtaining the plot shown in Fig. 4.

Data availability

References

1. Ghavamian, P., Schwartz, S. J., Mitchell, J., Masters, A. & Laming, J. M. Electron–ion temperature equilibration in collisionless shocks: the supernova remnant–solar wind connection. *Space Sci. Rev.* **178**, 633–663 (2013).
2. Landau, L. D. & Lifshitz, E. M. *Fluid Mechanics* (Pergamon, Oxford, 1959).
3. Bykov, A. M., Dolag, K. & Durret, F. Cosmological shock waves. *Space Sci. Rev.* **134**, 119–140 (2008).
4. Vink, J. Supernova remnants: the X-ray perspective. *Astron. Astrophys. Review* **20**, 49 (2012).
5. Tsurutani, B. T. & Stone, R. G. (eds) *Collisionless Shocks in the Heliosphere: Reviews of Current Research* Geophysical Monograph Series, Vol. 35 (American Geophysical Union, 1985).
6. Chevalier, R. A. & Raymond, J. C. Optical emission from a fast shock wave—the remnants of Tycho's supernova and SN 1006. *Astrophys. J.* **225**, L27–L30 (1978).
7. Chevalier, R. A., Kirshner, R. P. & Raymond, J. C. The optical emission from a fast shock wave with application to supernova remnants. *Astrophys. J.* **235**, 186–195 (1980).
8. Raymond, J. C. Shock waves in supernova ejecta. *Space Sci. Rev.* **214**, 28 (2018).
9. Rakowski, C. E., Ghavamian, P. & Hughes, J. P. The physics of supernova remnant blast waves. II. Electron–ion equilibration in DEM L71 in the Large Magellanic Cloud. *Astrophys. J.* **590**, 846–857 (2003).
10. van Adelsberg, M., Heng, K., McCray, R. & Raymond, J. C. Spatial structure and collisionless electron heating in balmer-dominated shocks. *Astrophys. J.* **689**, 1089–1104 (2008).
11. Ghavamian, P., Laming, J. M. & Rakowski, C. E. A physical relationship between electron-proton temperature equilibration and mach number in fast collisionless shocks. *Astrophys. J.* **654**, L69–L72 (2007).
12. Rakowski, C. E., Laming, J. M. & Ghavamian, P. The heating of thermal electrons in fast collisionless shocks: the integral role of cosmic rays. *Astrophys. J.* **684**, 348–357 (2008).
13. Vink, J., Broersen, S., Bykov, A. & Gabici, S. On the electron–ion temperature ratio established by collisionless shocks. *Astron. Astrophys.* **579**, A13 (2015).
14. Shimada, N. & Hoshino, M. Strong electron acceleration at high Mach number shock waves: simulation study of electron dynamics. *Astrophys. J.* **543**, L67–L71 (2000).
15. Park, J., Caprioli, D. & Spitkovsky, A. Simultaneous acceleration of protons and electrons at nonrelativistic quasiparallel collisionless shocks. *Phys. Rev. Lett.* **114**, 085003 (2015).
16. Korreck, K. E., Raymond, J. C., Zurbuchen, T. H. & Ghavamian, P. Far ultraviolet spectroscopic explorer observation of the nonradiative collisionless shock in the remnant of SN 1006. *Astrophys. J.* **615**, 280–285 (2004).
17. Berdichevsky, D., Geiss, J., Gloeckler, G. & Mall, U. Excess heating of $^4He^{2+}$ and O^{6+} relative to H^+ downstream of interplanetary shocks. *J. Geophys. Res.* **102**, 2623–2636 (1997).
18. Raymond, J. C., Winkler, P. F., Blair, W. P. & Laming, J. M. Ion–ion equilibration and particle distributions in a 3000 km s^1 shock in SN 1006. *Astrophys. J.* **851**, 12 (2017).
19. Broersen, S. et al. The northwestern ejecta knot in SN 1006. *Astron. Astrophys.* **552**, A9 (2013).
20. Vink, J., Laming, J. M., Gu, M. F., Rasmussen, A. & Kaastra, J. S. The slow temperature equilibration behind the shock front of SN 1006. *Astrophys. J.* **587**, L31–L34 (2003).
21. West, R. M., Lauberts, A., Schuster, H.-E. & Jorgensen, H. E. Astrometry of SN 1987A and Sanduleak-69 202. *Astron. Astrophys.* **177**, L1–L3 (1987).
22. McCray, R. Supernova 1987A revisited. *Annu. Rev. Astron. Astr.* **31**, 175–216 (1993).
23. McCray, R. & Fransson, C. The remnant of supernova 1987A. *Annu. Rev. Astron. Astr.* **54**, 19–52 (2016).
24. Orlando, S., Miceli, M., Pumo, M. L. & Bocchino, F. Supernova 1987A: a template to link supernovae to their remnants. *Astrophys. J.* **810**, 168 (2015).
25. Spitzer, L. *Physics of Fully Ionized Gases* 2nd edn (Interscience, New York, 1962).
26. Frank, K. A. et al. Chandra observes the end of an era in SN 1987A. *Astrophys. J.* **829**, 40 (2016).
27. Zhekov, S. A., McCray, R., Borkowski, K. J., Burrows, D. N. & Park, S. Chandra observations of shock kinematics in supernova remnant 1987A. *Astrophys. J.* **628**, L127–L130 (2005).
28. Zhekov, S. A. et al. High-resolution X-ray spectroscopy of SNR 1987A: Chandra LETG and HETG observations in 2007. *Astrophys. J.* **692**, 1190–1204 (2009).
29. Dewey, D., Dwarkadas, V. V., Haberl, F., Sturm, R. & Canizares, C. R. Evolution and hydrodynamics of the very broad X-ray line emission in SN 1987A. *Astrophys. J.* **752**, 103 (2012).
30. Caprioli, D., Yi, D. T. & Spitkovsky, A. Chemical enhancements in shock-accelerated particles: ab initio simulations. *Phys. Rev. Lett.* **119**, 171101 (2017).
31. Zanardo, G. et al. Detection of linear polarization in the radio remnant of supernova 1987A. *Astrophys. J.* **861**, L9 (2018).
32. Narayan, R. & Medvedev, M. V. Thermal conduction in clusters of galaxies. *Astrophys. J.* **562**, L129–L132 (2001).
33. France, K. et al. HST-COS observations of hydrogen, helium, carbon, and nitrogen emission from the SN 1987A reverse shock. *Astrophys. J.* **743**, 186 (2011).
34. Orlando, S., Drake, J. J. & Laming, J. M. Three-dimensional modeling of the asymmetric blast wave from the 2006 outburst of RS Ophiuchi: early X-ray emission. *Astron. Astrophys.* **493**, 1049–1059 (2009).
35. Miceli, M., Orlando, S., Reale, F., Bocchino, F. & Peres, G. Hydrodynamic modelling of ejecta shrapnel in the Vela supernova remnant. *Mon. Not. R. Astron. Soc.* **430**, 2864–2872 (2013).
36. Park, S. et al. Evolutionary status of SNR 1987A at the age of eighteen. *Astrophys. J.* **646**, 1001–1008 (2006).
37. Sugerman, B. E. K., Crotts, A. P. S., Kunkel, W. E., Heathcote, S. R. & Lawrence, S. S. The three-dimensional circumstellar environment of SN 1987A. *Astrophys. J. Suppl. S.* **159**, 60–99 (2005).
38. Dewey, D., Zhekov, S. A., McCray, R. & Canizares, C. R. Chandra HETG spectra of SN 1987A at 20 years. *Astrophys. J.* **676**, L131 (2008).

Author contributions

M.M. composed the text on the basis of inputs from all authors. M.M. designed the analysis procedure and led the analysis of the synthetic and actual X-ray spectra. S.O. led the set-up and run of the hydrodynamics simulation and the synthesis of X-ray spectra. D.N.B., K.A.F. and C.A. supported the X-ray data analysis process. F.R., G.P., O.P. and F.B. supported the analysis of the simulation and the synthesis of observables. All authors helped to discuss the results and to comment on the manuscript.

Competing interests

The authors declare no competing interests.

Additional information